Hybrid Model Predictive Power Flow Control of a Fuel Cell-Battery Vehicle

Richard Meyer[*], Raymond A. DeCarlo[†], Peter H. Meckl[*], Chris Doktorcik[†], and Steve Pekarek[†]

[*] School of Mechanical Engineering
Purdue University, West Lafayette, Indiana 47907
Email: rtmeyer@purdue.edu
[†] School of Electrical and Computer Engineering
Purdue University, West Lafayette, Indiana 47907

Abstract— This paper considers optimal power flow control of a fuel cell-battery hybrid vehicle (FCHV) powertrain having three distinct modal configurations (modes): electric motor propelling/battery discharging, propelling/charging, and generating/charging. Each mode has a distinct set of dynamics and constraints. Using component dynamical/algebraic models appropriate to power management, the paper develops a supervisory-level switched system model as an interconnection of subsystems. Given the model, the paper sets forth a hybrid model predictive control strategy based on a minimization of a performance index (PI) that trades off tracking and fuel economy in each operational mode. Specifically the PI trades off velocity tracking error, battery state of charge variance, and hydrogen usage while penalizing frictional braking. The optimization is performed using an embedded system model and collocation with MATLAB's fmincon to compute mode switches and continuous time controls thereby avoiding the computational complexity of alternate approaches based on, e.g., mixed integer programming. To demonstrate the approach, an example FCHV following trapezoidal and sawtooth drive profiles is simulated. PI weights are varied for reduced hydrogen use and higher final battery charge to illustrate various performance trade-offs.

I. INTRODUCTION

The fuel cell-battery hybrid vehicle (FCHV) powertrain shown in Fig. 1 is capable of operating in three power flow modes: electric motor propelling and battery discharging; motor propelling and battery charging; and motor generating and battery charging. Past supervisory-level power control work either does not include discrete-valued modes as a control input [1], [2], [3] or does so at the expense of requiring mixed-integer linear programming to find the control [4]. Mode control is integral to optimal power management and, through the embedding approach [5], solvable with traditional nonlinear programming. Herein, the switched power flow problem is formed into an embedded optimal control problem (EOCP) that simultaneously contains all three of the power flow modes described. The EOCP solution is then parlayed into a specific mode and its power control inputs using a projection approach developed herein. Simulation results are presented for a mid-size sedan FCHV following trapezoidal and sawtooth shaped drive profiles.

II. POWER FLOW COMPONENT AND SYSTEM MODELS

Fig. 1 shows the powertrain components and their electrical and/or mechanical interconnections. The component models are tailored to supervisory-level power flow management as opposed to detailed first principles models.

A. Components

1) Fuel Cell System: The H_2/air fuel cell system (FCS) consists of a proton exchange membrane stack and supporting balance of plant components. The FCS used is similar to that in [1], [6], except air is supplied from a low-pressure blower [7]. The FCS is capable of producing 55 kW during normal operation at 80°C and 12.5 kPa gauge. The net output power flow is approximated by a first-order lag equation:

$$\frac{dP_{fc,net}(t)}{dt} = \frac{1}{\tau_{fc}}[-P_{fc,net}(t) + P_{fc,net}^{max}u_{fc}(t)] \qquad (1)$$

where $P_{fc,net}$ is the fuel cell net power, $P_{fc,net}^{max}$ is the maximum available output power at the operating conditions, $u_{fc} \in [0,1]$ is the normalized actuation, and τ_{fc} is the time constant of the power response. This approach is similar to the diesel engine model adopted in [8]. The time constant for the controlled stack's power output in [1], [6] is estimated to be 0.25 s but rapid changes in desired power promote fuel cell catalyst degradation and a reduced life [9]. τ_{fc} is chosen as 1.375 s, ensuring the desired power response is feasible and preventing potential damage to the fuel cell by limiting the zero to 55 kW fuel cell response to an average change of 10 kW/s.

The FCS input power is the rate of H_2 chemical energy consumed to provide the net output power:

$$P_{H_2}(t) = \frac{P_{fc,net}(t)}{\eta_{fc}(P_{fc,net}(t))} \qquad (2)$$

where the efficiency from [1], [6], [7] is functionally approximated with

$$\eta_{fc}(P_{fc,net}) =$$
$$\begin{cases} 0.456\left[\exp(-3.24 \cdot 10^{-3}P_{fc,net})\right. \\ \left. - \exp(-0.935P_{fc,net})\right], & 0 \leq P_{fc,net} < 41.5 \text{ kW} \\ -2.88 \cdot 10^{-5}P_{fc,net}^3 + 3.58 \cdot 10^{-3}P_{fc,net}^2 \\ -0.150P_{fc,net} + 2.511, & P_{fc,net} \geq 41.5 \text{ kW}. \end{cases} \qquad (3)$$

2) Battery: The battery state of charge (SOC), $\overline{W}_{bat}$, dynamic model is based on a validated empirical formula [10], [11] with battery power input, P_{bat}; the formula is modified to include an additional quadratic battery power term in the efficiency relation so as to better represent the available battery data of the Lithium-Ion module used herein. The model is linearized about P_{bat}^{nom} to obtain a model affine in the control input (to satisfy a condition for the existence of an EOCP optimal solution [5]):

$$\frac{d\overline{W}_{bat}(t)}{dt} = \frac{1}{W_{bat}^{max}}\left\{d_2^{v_b}(P_{bat}^{nom,v_b})^2 + 2d_4^{v_b}(P_{bat}^{nom,v_b})^3 \right.$$
$$- \left[k^{v_b}\ln(\overline{W}_{bat}(t) + d_1^{v_b}) + 2d_2^{v_b}P_{bat}^{nom,v_b}\right.$$
$$\left.\left. + d_3^{v_b} + 3d_4^{v_b}(P_{bat}^{nom,v_b})^2\right]P_{bat}(t)\right\} \qquad (4)$$

where $v_b = 0$, $P_{bat} \geq 0$, for discharge and $v_b = 1$, $P_{bat} \leq 0$, for charge, $d_i^{v_b}$ are discharging/charging fit coefficients, and W_{bat}^{max} is the battery's maximum rated storage energy. The battery pack is composed of 27 Saft 10.8 V, 12 Ah Lithium-Ion modules [12], [13] with $\overline{W}_{bat} \in [0.4, 0.8]$, W_{bat}^{max} of 3.8 kWh (13680 kWs
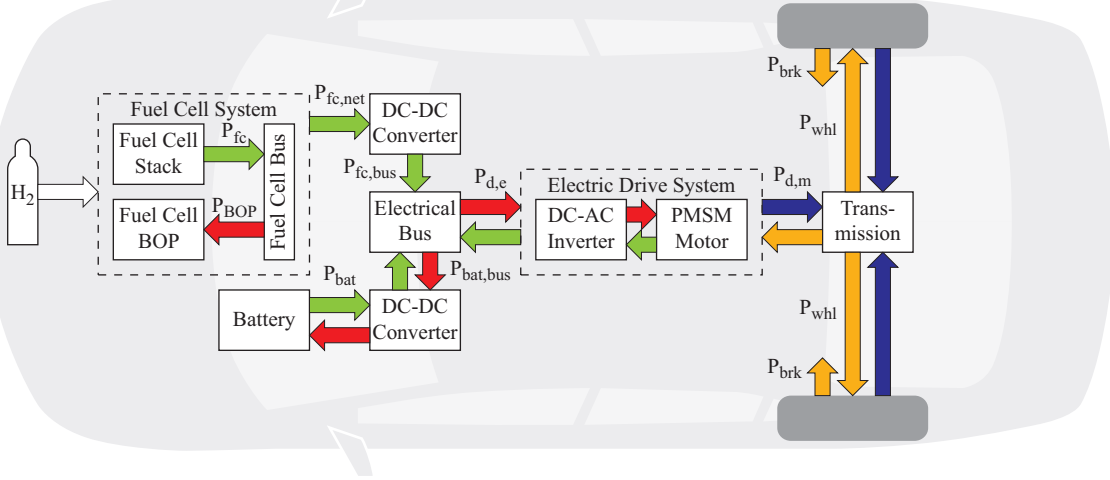
Fig. 1. Fuel cell hybrid vehicle powertrain potential power flows: (🟩) electrical power produced, (🟥) electrical power consumed, (🟦) mechanical power produced, (🟧) mechanical power consumed, (⬜) H_2 input. (BOP is the balance of plant.)

in (4)), and maximum discharge/charge of $40.5/-40.5$ kW while above the minimum voltage limit. The $d_i^{v_b}$ coefficients are obtained from fitting ADVISOR [13] battery data: (discharging) $d_1^0 = 3.91$, $d_2^0 = -3.28 \cdot 10^{-3}$, $d_3^0 = 2.57$, $d_4^0 = 3.92 \cdot 10^{-2}$, and $k^0 = -1$; (charging) $d_1^1 = 2.57 \cdot 10^1$, $d_2^1 = 5.20 \cdot 10^{-3}$, $d_3^1 = -2.27$, $d_4^0 = 3.25 \cdot 10^{-5}$, and $k^1 = 1$; and the nominal discharge/charge battery power is $10/-10$ kW.

3) Electric Drive System: The electric drive system (EDS) consists of a DC-AC inverter and permanent magnet synchronous motor that act as either a motor or generator. The EDS is modeled algebraically using input-to-output power efficiency maps. During propelling

$$P_{d,e}(t) = P_{d,e}^{max,p}(\omega_d)u_d^0(t) \tag{5}$$

$$P_{d,m}(t) = \eta_d^p(P_{d,m}, \omega_d)P_{d,e}(t) \tag{6}$$

and during generating

$$P_{d,e}(t) = \eta_d^g(P_{d,e}, \omega_d)P_{d,m}(t) \tag{7}$$

$$P_{d,m}(t) = P_{d,m}^{max,g}(\omega_d)u_d^1(t) \tag{8}$$

where $P_{d,e}/P_{d,m}$ is the drive electrical/mechanical power, ω_d is the angular shaft speed, η_d^p/η_d^g is the propelling/generating power transfer efficiency, and $u_d^{v_d}(t) \in [0, 1]$ controls the motoring, $v_d = 0$, or generating, $v_d = 1$, power input. The EDS is a UQM Power-Phase 100 [14] with maximum mechanical power of 100 kW and minimum electrical generating speed of 4.7 rad/s. Table I gives approximate η_d^p and η_d^g extrapolated from manufacturer operational data. Propelling "efficiency" is nonzero at $\omega_d = 0$ which makes the power management problem well-posed, i.e., nonzero power in produces nonzero power out, however $\eta_d^p(P_{d,m}, \omega_d = 0) = 0$ is typically expected. Thus, we assert η_d^p is valid for $\omega_d > 5$ rad/s, the lower limit of the given data, and for the solvability of the power management problem apply $\eta_d^p \approx 0.7$ at $\omega_d = 0$ from the fit of the data. In other words, we accept the nonzero propelling efficiency at $\omega_d = 0$ to avoid a more complicated supervisory-level EDS power flow model with the recognition that the η_d^p value at $\omega_d = 0$ does not truly represent the actual efficiency of the drive at this condition. Maximum propelling and generating input powers

TABLE I
EDS POWER EFFICIENCY

Parameter	Propelling	Generating
C_1	$-3.44 \cdot 10^{-5}$ kW^{-2}	$-4.54 \cdot 10^{-5}$ kW^{-2}
C_2	$6.58 \cdot 10^{-6}$ s/(rad kW)	$6.74 \cdot 10^{-6}$ s/(rad kW)
C_3	$-1.88 \cdot 10^{-6}$ s^2/rad^2	$-2.69 \cdot 10^{-6}$ s^2/rad^2
C_4	$3.57 \cdot 10^{-3}$ kW^{-1}	$3.85 \cdot 10^{-3}$ kW^{-1}
C_5	$6.99 \cdot 10^{-4}$ s/rad	$1.21 \cdot 10^{-3}$ s/rad
C_6	0.688	0.639
$\eta_d^g, \eta_d^p = C_1 P_{out}^2 + C_2 P_{out}\omega_d + C_3\omega_d^2 + C_4 P_{out} + C_5\omega_d + C_6$		
$\eta_d^g = 0, \quad 0 \leq \omega_d \leq 4.7$		

(in kW) are $\mathcal{C}^1$ functions of ω_d derived from manufacturer data:

$$P_{d,e}^{max,p}(\omega_d), P_{d,m}^{max,g}(\omega_d) =$$

$$\begin{cases} C_{13}\omega_d^3 + C_{12}\omega_d^2 + C_{11}\omega_d + C_{10}, & 0 \leq \omega_d \leq 50\pi \\ C_{24}\omega_d^4 + C_{23}\omega_d^3 + C_{22}\omega_d^2 + C_{21}\omega_d + C_{20}, & 50\pi < \omega_d \leq \frac{200\pi}{3} \\ C_{32}\omega_d^2 + C_{31}\omega_d + C_{30}, & \frac{200\pi}{3} < \omega_d \leq 150\pi. \end{cases} \tag{9}$$

For $P_{d,e}^{max,p}$, ignoring C_{ij} units, $C_{13} = 5.75 \cdot 10^{-6}$, $C_{12} = -1.65 \cdot 10^{-3}$, $C_{11} = 0.711$, $C_{10} = 3.58$, $C_{24} = 1.67 \cdot 10^{-7}$, $C_{23} = -1.11 \cdot 10^{-4}$, $C_{22} = 2.08 \cdot 10^{-2}$, $C_{21} = -0.278$, $C_{20} = -43.29$, $C_{32} = 1.60 \cdot 10^{-4}$, $C_{31} = -0.119$, and $C_{30} = 1.29 \cdot 10^2$. For $P_{d,m}^{max,g}$, $C_{11} = 0.550$, $C_{23} = 1.10 \cdot 10^{-5}$, $C_{22} = -1.13 \cdot 10^{-2}$, $C_{21} = 3.29$, $C_{20} = -1.94 \cdot 10^2$, $C_{30} = 100$, and all other $C_{ij} = 0$.

4) DC-DC Converters and Electrical Bus: The electrical bus serves as the power transfer point between the FCS, battery, and EDS. The FCS is connected to the electrical bus with a unidirectional DC-DC converter while the battery is attached via a bidirectional DC-DC converter. The converters are modeled with constant efficiencies at the supervisory-level; these include any electrical bus losses as well. Both $\eta_{dcc,fc}$ and $\eta_{dcc,bat}$ are set to 0.92. The EDS is directly connected to the bus and any electrical bus connection losses are assumed part of the converter efficiencies. The result is that the electrical bus is treated as having unit power transfer efficiency and the power flow across the bus is conserved.

5) Mechanical Transmission: The EDS's motor output shaft is connected to the traction wheels through a fixed ratio transmission.

The power transfer relationship is

$$P_{whl}(t) = \begin{cases} \eta_{mt} P_{d,m}(t), & v_d = 0 \\ \frac{-P_{d,m}(t)}{\eta_{mt}}, & v_d = 1 \end{cases} \qquad (10)$$

where P_{whl} is the propelling or regenerative braking power, and η_{mt} is the transmission efficiency. Here, the transmission between the EDS motor shaft and wheels is ideal with an efficiency of one. The transmission gear ratio is 3.6, giving the motor speed to vehicle speed as $\omega_d = 3.6V/r_{whl}$ with wheel radius r_{whl}.

6) Vehicle: The vehicle consumes power during propelling or can generate it while slowing. A point-mass, linear motion dynamics model is applied:

$$\begin{aligned} \frac{dV(t)}{dt} =& \frac{1}{m_v} \left(F_d(V) + F_{rr}(V, \alpha) + F_b(\alpha) \right) \\ &+ \frac{1000 \left[P_{whl}(t) - P_{brk}(t) \right]}{m_v(V(t) + \epsilon_V)} \\ F_d(V) =& -0.5 \rho_{air} A_{fr} C_d V(t)^2 \text{sgn}(V(t)) \\ F_{rr}(V, \alpha) =& -C_{rr} m_v g \cos(\alpha) \text{sgn}(V(t)) \\ F_b(\alpha) =& -m_v g \sin(\alpha) \end{aligned} \qquad (11)$$

where ρ_{air} is the ambient air density, A_{fr} is the vehicle frontal area, C_d is the drag coefficient, C_{rr} is the tire rolling resistance, α is the road grade angle, $\epsilon_V = 0.3$ prevents division by zero when stopped, and $P_{brk}(t)$ is the frictional braking power. The braking power [8], [10] is equal to a velocity dependent maximum braking power scaled by $u_{brk}(t) \in [0, 1]$:

$$P_{brk}(t) = P_{brk}^{max}(V) u_{brk}(t) \qquad (12)$$

$$P_{brk}^{max}(V) = 50 \tanh \left(\frac{V(t)}{5} \right). \qquad (13)$$

The vehicle is a mid-size passenger sedan: A_{fr}=2.35 m^2, C_d=0.3, C_{rr}=0.009, m_v=1800 kg (1600 kg curb weight+200 kg cargo), and r_{whl}=0.322 m. The vehicle parameters are averaged from the Ford Fusion hybrid, Honda Accord hybrid and FCX Clarity, and Toyota Camry and Prius hybrids.

B. System Modes

The power flow between components is capable of taking three unique configurations: mode 0-motor propelling/battery discharging, mode 1-motor propelling/battery charging, and mode 2-motor generating/battery charging. Each of the three system modes has a unique set of dynamic and algebraic relations that describe the power flow. The system power flow model is the mode-switched amalgamation of all three modes. The mode switch (control) vector $v(t) = (v_0(t), v_1(t), v_2(t))$ dictates which mode relation set is active; the components satisfy $v_i(t) \in \{0, 1\}$ and

$$v_0 + v_1 + v_2 = 1 \qquad (14)$$

which restricts operation to a single mode at a time.

C. System Model

The dynamics from (1), (4), and (11) are combined into a switched system representation using the components of the mode control vector, v:

$$\begin{bmatrix} \dot{P}_{fc,net} \\ \overline{\dot{W}}_{bat} \\ \dot{V} \end{bmatrix} = v_0 \begin{bmatrix} f_{fc}(P_{fc,net}, u_{fc}^0) \\ f_{bat}^d(\overline{W}_{bat}, P_{bat}^0) \\ f_V(V, P_{brk}^0, P_{whl}^0) \end{bmatrix} + v_1 \begin{bmatrix} f_{fc}(P_{fc,net}, u_{fc}^1) \\ f_{bat}^c(\overline{W}_{bat}, P_{bat}^1) \\ f_V(V, P_{brk}^1, P_{whl}^1) \end{bmatrix}$$
$$+ v_2 \begin{bmatrix} f_{fc}(P_{fc,net}, u_{fc}^2) \\ f_{bat}^c(\overline{W}_{bat}, P_{bat}^2) \\ f_V(V, P_{brk}^2, P_{whl}^2) \end{bmatrix}. \qquad (15)$$

Every mode has a set of dynamics associated with it that produce the system response when that mode is active (mode switch equal to one). The inputs to a mode's set of dynamics are unique even if it includes dynamics duplicated in other modes. For example, the FCS response (1) is common to all modes and the input u_{fc} is not presented as mode specific, but u_{fc}^0 u_{fc}^1, or u_{fc}^2 is applied in the respective mode. These input distinctions are consistent with the switching control and are necessary to the embedded control problem (defined shortly). The continuous control inputs defined for each mode are

$$u^0 = [u_{brk}^0, u_d^{p0}, u_{fc}^0]^T \qquad (16)$$
$$u^1 = [u_{brk}^1, u_d^{p1}, u_{fc}^1]^T \qquad (17)$$
$$u^2 = [u_{brk}^2, u_d^{g2}, u_{fc}^2]^T. \qquad (18)$$

Each mode also shares dynamic states, x, and there are six algebraic power variables per mode: P_{bat}^i, P_{brk}^i, $P_{d,e}^i$, $P_{d,m}^i$, P_{H_2}, and P_{whl}^i. Additionally, (2) is included with the system performance index defined in the next section, as opposed to being part of the model, to determine and "minimize" H$_2$ consumption during the optimization.

D. System Interconnections

The following constraints from the component development are the interconnection equations [15] for each mode of operation. The mode 0 algebraic constraints for the electrical bus (19), EDS electrical (20) and mechanical (21), mechanical transmission (22), and braking (23) are

$$P_{d,e}^0 = \eta_{dcc,fc} P_{fc,net} + \eta_{dcc,bat} P_{bat}^0 \qquad (19)$$
$$P_{d,e}^0 = P_{d,e}^{max,p}(V) u_d^{p0} \qquad (20)$$
$$P_{d,m}^0 = \eta_d^p(P_{d,m}^0, V) P_{d,e}^0 \qquad (21)$$
$$P_{whl}^0 = P_{d,m}^0 \qquad (22)$$
$$P_{brk}^0 = P_{brk}^{max}(V) u_{brk}^0. \qquad (23)$$

The mode 1 algebraic constraints for the electrical bus (24), EDS electrical (25) and mechanical (26), mechanical transmission (27), and braking (28) are

$$P_{d,e}^1 - \frac{P_{bat}^1}{\eta_{dcc,bat}} = \eta_{dcc,fc} P_{fc,net} \qquad (24)$$
$$P_{d,e}^1 = P_{d,e}^{max,p}(V) u_d^{p1} \qquad (25)$$
$$P_{d,m}^1 = \eta_d^p(P_{d,m}^1, V) P_{d,e}^1 \qquad (26)$$
$$P_{whl}^1 = P_{d,m}^1 \qquad (27)$$
$$P_{brk}^1 = P_{brk}^{max}(V) u_{brk}^1. \qquad (28)$$

The mode 2 algebraic constraints for the electrical bus (29), EDS electrical (30) and mechanical (31), and mechanical transmission (32), and braking (33) are

$$\frac{-P_{bat}^2}{\eta_{dcc,bat}} = \eta_{dcc,fc} P_{fc,net} + P_{d,e}^2 \qquad (29)$$
$$P_{d,e}^2 = \eta_d^g(P_{d,e}^2, V) P_{d,m}^2 \qquad (30)$$
$$P_{d,m}^2 = P_{d,m}^{max,g}(V) u_d^{g2} \qquad (31)$$
$$P_{whl}^2 = -P_{d,m}^2 \qquad (32)$$
$$P_{brk}^2 = P_{brk}^{max}(V) u_{brk}^2. \qquad (33)$$

III. CONTROL

A. Switched Optimal Control Problem

The switched optimal control problem (SOCP) is to determine the active mode switching, $v_i \in \{0, 1\}$, and continuous power

flow control inputs for velocity profile tracking, fuel economy, and battery health. Specifically, the MPC problem is

$$\min_{u^0,u^1,u^2,v} J(x_0,t_0,u^0,u^1,u^2,v) \qquad (34)$$

subject to the constraints from (2), (14), (15), and (19)-(33), where the performance index (PI) is

$$
\begin{aligned}
J = &\int_{t_0}^{t_f} C_{bat}(\overline{W}_{bat}(t) - \overline{W}_{bat,des})^2 \mathrm{d}t \\
&+ \int_{t_0}^{t_f} C_V (V(t) - V_{ref}(t))^2 \mathrm{d}t \\
&+ \int_{t_0}^{t_f} C_{H_2} \left(\frac{P_{H_2}(t)}{P_{H_2}^{max}} \right)^2 \mathrm{d}t \\
&+ \int_{t_0}^{t_f} C_{brk} \sum_{i=0}^{2} v_i \left(\frac{P_{brk}^i(t)}{P_{brk}^{max}(V_{max})} \right)^2 \mathrm{d}t,
\end{aligned}
\qquad (35)
$$

and $[t_0, t_f]$ is the control prediction horizon. The penalty on P_{brk}^i, frictional braking, is included to promote battery recharging when there is an excess of vehicle kinetic energy. Fuel use is minimized, i.e., economy is maximized, through the P_{H_2} cost term as P_{H_2} is directly proportional to the mass flow rate of H$_2$.

Solving the above FCHV powertrain SOCP usually requires mixed-integer programming [4], whose computational complexity is NP-hard and exponentially increases with the number of modes [16]. This approach is circumvented by recasting the switched problem into the embedded (hybrid) optimal control problem (EOCP).

B. Embedded Optimal Control Problem

The embedded optimal control problem (EOCP) is formed by recasting the v_i terms in $v(t) \in \{0,1\} \times \{0,1\} \times \{0,1\}$ as real numbers in the interval [0,1]. This embeds the SOCP into a larger family of systems. We denote the new switching vector by $\tilde{v}(t)$, where $\tilde{v}_i \in [0,1]$ and $\tilde{v}$ inheriting all other conditions on $v(t)$ [5]. The EOCP objective becomes

$$\min_{\tilde{u},\tilde{v}} J(x_0,t_0,\tilde{u},\tilde{v}) \qquad (36)$$

over all constraints regardless of mode, where $\tilde{u}$ contains the continuous control inputs associated with the embedded system. Bengea and DeCarlo [5] give sufficient conditions for an optimal solution of the EOCP to exist: the dynamical system equations (vector fields) are linear in the continuous control inputs and the PI is convex in these same inputs. This is satisfied by the given model and performance index. This means that there exists at least a (possibly non-unique) global minimum.

References [5], [10], [16], [17], [18] demonstrate that the EOCP is an effective and efficient means for computing solutions to the SOCP as it is amenable to traditional nonlinear programming techniques since the switched system trajectories are dense in the embedded system trajectories. The latter means that either the optimal EOCP solution contains the optimal SOCP solution or that the embedded optimal solution can be approximated by an SOCP solution to any arbitrary degree. (The point being that the embedded solution is the infimum of any SOCP solutions.) If all optimal $\tilde{v} \in \{0,1\}$, then the EOCP and SOCP solutions are the same. However, if any optimal $\tilde{v} \in (0,1)$, the construction of the approximating SOCP solution must determine (i) which mode should be active (termed mode projection), and (ii) the values of the continuous control inputs in the projected mode of operation.

1) Mode Projection: The first step in approximating the optimal EOCP solution with an SOCP solution is to project the embedded modes within an interval onto a single active switched mode such that $v_I = 1$ and $v_i = 0 \, \forall i \neq I$. To start mode projection, a decision variable is calculated for each mode; it is the $\tilde{v}_i$ weighted 2-norm of a power set that includes both the mode's commanded powers and unique, mode-specific powers:

$$N^i = \tilde{v}_i \| [P_{fc,net}^i, P_{bat}^i, P_{brk}^i, P_{d,e}^i, P_{d,m}^i] \|_2, \quad i = 0, 1, 2 \quad (37)$$

where $P_{fc,net}^i = P_{fc,net}^{max} u_{fc}^i$ is introduced so as to include the mode's commanded (steady-state) fuel cell power. P_{whl}^i is not included because it is equal in magnitude to $P_{d,m}^i$ and doesn't provide new information. And P_{H_2} and $P_{fc,net}$ are absent as they are not mode specific. The 2-norm is weighted by $\tilde{v}^i$ to account for the relative affect of a mode's powers on the embedded system response. To choose the projected mode using the decision variables, the N^i are arranged into a nonincreasing sequence $\{N^a, N^b, N^c\}$ and the active mode is selected as (i) a if $N^a > N^b$; (ii) the most recently active a or b mode if $N^a = N^b > N^c$; (iii) the previous sample interval's active mode if $N^a = N^b = N^c$.

2) Control Projection: With the modes selected, the applied control inputs are found next to complete the suboptimal SOCP solution. If a control input is not affected by $\tilde{v}$, then it is applied directly. However, if the EOCP solution for the control input j for mode i, $\tilde{u}_j^i$, is scaled by $\tilde{v}_i$ in the system dynamics, then the applied control in the selected mode is

$$u_j^i = \tilde{v}_i \tilde{u}_j^i. \qquad (38)$$

If these controls will give negative P_{bat} in mode 0 or positive P_{bat} in mode 1, then the nearest-valued, valid controls that do not result in the constraint violation are used. Controls in inactive modes are set to zero. This approach had been found experimentally (in a variety of simulation studies with diverse systems) to yield the best results short of resolving the optimization for the given mode or mode sequence. Theoretical research is ongoing.

The projected control derived from the EOCP solution is designated the projected embedded control (PEC).

IV. RESULTS

The control of a FCHV with PEC is demonstrated with a mid-size sedan following trapezoidal and sawtooth drive profiles (in Fig. 2). EPA profiles have been simulated with equivalently good results but are beyond the scope of this paper. Simulation results herein are from a differential algebraic solution to the switched system driven by the PEC inputs.

A. Problem Setup

The MPC prediction horizon is 2 s with a sample period of 1 s which results in a series of locally optimal controls applied over the length of the drive profile. The continuous system is discretized using orthogonal collocation with triangular basis functions [16]; the PI is approximated using trapezoidal numerical integration. PI weights are chosen to trade off fuel economy, battery maintenance, and velocity tracking: $C_{brk} = 100$, $C_{H_2} = 10$, and $C_V = 150$. C_{bat} varies with $\Delta\overline{W}_{bat}(t_0) = \overline{W}_{bat}(t_0) - \overline{W}_{bat,des}$, the difference between the most recent battery SOC and the desired value:

$$C_{bat} = \begin{cases} 600 \left(1 + 2225 |\Delta\overline{W}_{bat}(t_0)| \right), & \Delta\overline{W}_{bat}(t_0) \leq 0 \\ 0, & \Delta\overline{W}_{bat}(t_0) > 0. \end{cases} \qquad (39)$$

The desired battery SOC is 0.6. Below the desired SOC, battery usage is increasingly penalized. Above the desired SOC, the battery
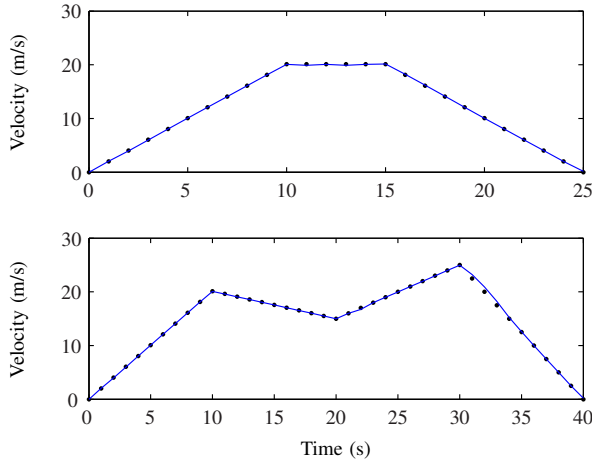
Fig. 2. Simulated vehicle velocity over the trapezoidal drive cycle (upper) and sawtooth profile (lower): (●) desired velocity, (—) simulated velocity.
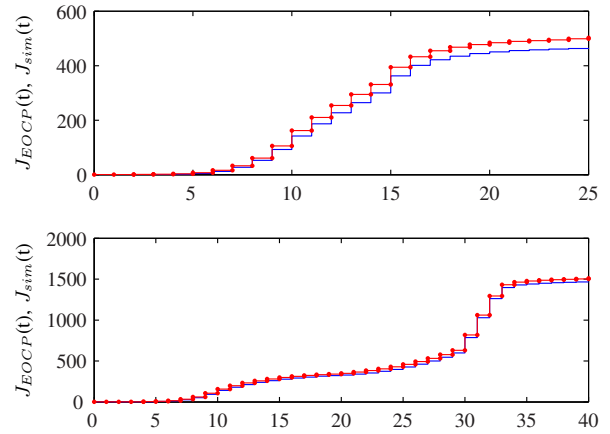

Fig. 3. Simulated performance index cost over the trapezoidal drive cycle (upper) and sawtooth drive cycle (lower) for the EOCP and simulated PEC results: (—) EOCP, (●) simulation.

is freely available for either usage or storage up to a maximum safe SOC of 0.8.

The battery SOC penalty herein may result in a more conservative local battery usage (and more fuel use) in comparison to keeping the horizon length equal to the drive time remaining and only penalizing the battery SOC deviation at the terminal time. In this case, the controller has, in general, more choice of when to best use the fuel cell to propel and/or charge the battery to reach the desired final SOC. This approach is computationally more expensive and requires *a priori* knowledge of the drive profile, which is not assumed here.

Reference velocities are linearly extrapolated over the prediction horizon from the vehicle speed at $t(k)$ and the current driver demand for $t(k+1)$.

$$V_{ref}(t) = V(t(k)) + \frac{V_{ref}(t(k+1)) - V(t(k))}{t(k+1) - t(k)} t \quad (40)$$

Equation 40 takes advantage of the natural ability of the driver to predict, through vision, near-term velocity requirements.

B. Drive Profile Tracking

Fig. 2 shows the excellent trapezoidal and sawtooth profile tracking results achieved. The 2-norm normalized velocity tracking error is 0.60% and 1.38% for the trapezoidal and sawtooth profiles respectively.

The PI cost over the drive cycles for the EOCP and PEC simulation are shown in Fig. 3. The curves verify the near optimality of the PEC since the EOCP solution is always optimal.

1) Trapezoidal Drive Profile: Fig. 4 displays the EOCP and projected mode values during the trapezoidal profile. Mode projection or suboptimal SOCP solutions are needed during approximately 40% of the drive cycle. The modes selected are reasonable for the drive profile. During increasing velocity on [0,10]s, the powertrain is propelling the vehicle while utilizing the battery to help drive it, saving H_2 while the battery SOC is still high. Next, during the constant reference velocity segment, several different modes are selected to keep the vehicle moving and also charge the battery. Lastly, during the reference deceleration, vehicle kinetic energy is favored as a charge source for the battery. A comparison of N^0, N^1, and N^2, the mode projection decision variables, on [0,3]s and [19,20]s reveals the chosen mode's N^i to be at least
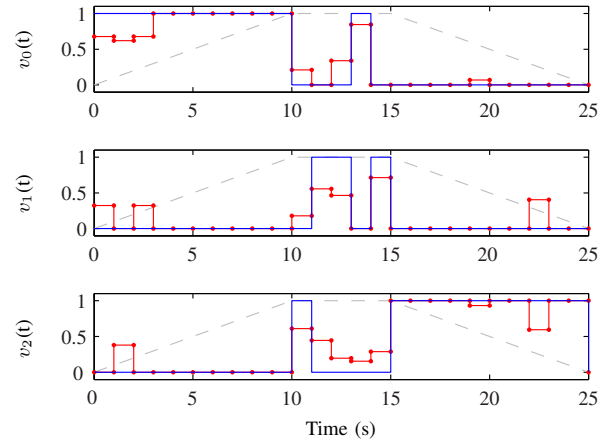
Fig. 4. Trapezoidal profile embedded and projected mode values: (—) projected, PEC; (●) embedded, EOCP; (– –) superimposed drive profile.

two orders of magnitude greater than the others. Over [10,15]s and [22,23]s the nonzero decision values are closer, with the smallest difference, 27%, on [11,12]s. During reference profile acceleration and deceleration, modes 0 and 2 are the better choices, respectively; but during constant velocity each mode is valuable.

Fig. 5 gives the FCS net power and battery SOC responses for the embedded problem and simulation. During the simulation, a maximum value of 49.6 kW is achieved, while the maximum rate of increase is 10 kW/s. The low rate of power change helps to extend the fuel cell life and reduce performance degradation over time. The fuel economy during the simulated drive cycle is 2.15 kg H_2/100 km. The simulated and EOCP FCS powers vary the most from 10 to 15 s and 22 to 23 s, the same interval upon which the nonzero mode projection decision values, N^i, are least different (recall the smallest difference is 27%). For other projection times, when the applied mode's N^i is much greater than the rest, the variation in powers is not as significant. This suggests that when the nonzero N^i are similar, it is harder to approximate the EOCP FCS response when limited to a single mode. However, the battery SOC of the embedded problem and simulation are nearly identical at all times; it is less sensitive to mode projection. The initial battery
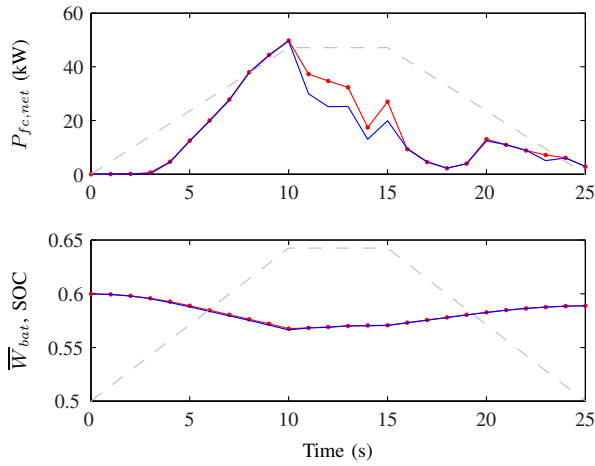
Fig. 5. Fuel cell system net power (upper) and battery SOC (lower) response during the trapezoidal drive cycle: (—) PEC simulation, (●) EOCP, (– –) superimposed drive profile.
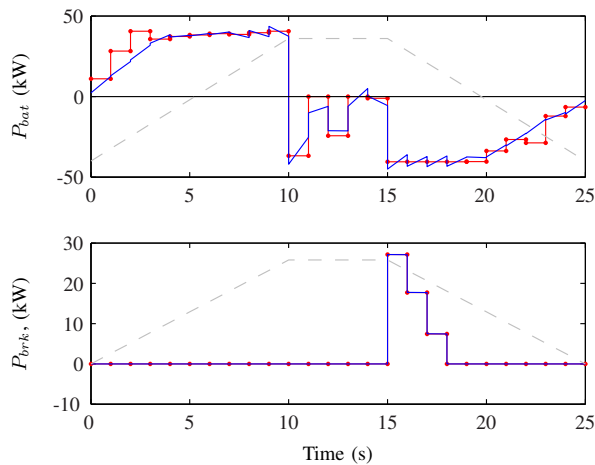

Fig. 6. Battery power (upper) and friction braking (lower) over the trapezoidal drive cycle: (—) PEC simulation, (●) EOCP, (– –) superimposed drive profile.

Fig. 7. Sawtooth profile embedded and projected mode values: (—) projected, PEC; (●) embedded, EOCP; (– –) superimposed drive profile.

Fig. 8. Fuel cell system net power (upper) and battery SOC (lower) response during the sawtooth drive cycle: (—) PEC simulation, (●) EOCP, (– –) superimposed drive profile.

SOC response shows that its usage is preferred over the fuel cell when the SOC is near the desired value of 0.6. Also, the control drives the battery SOC back toward the desired value using both the fuel cell and vehicle kinetic energy when the drive profile does not require acceleration. The simulation final SOC is 0.5889, a difference of 1.85% from the $\overline{W}_{bat,des}$ of 0.6.

Fig. 6 displays the battery power and frictional braking over the trapezoidal drive cycle. Battery energy is drained while the vehicle is accelerating during [0,10]s. The control takes full advantage of the requested deceleration from 15 to 25 s, allocating the maximum charging power to the battery for as long as it can. The embedded problem and simulation battery powers are most different when mode projection is used since battery power is a function of the FCS and EDS control inputs, both of which change with projection. Also, frictional braking only occurs during mode 2, when the battery charge power limit is reached.

2) Sawtooth Drive Profile: Fig. 7 displays the projected and embedded mode switching during the sawtooth drive profile. Throughout the profile's acceleration segments, the mode chosen by the control is mode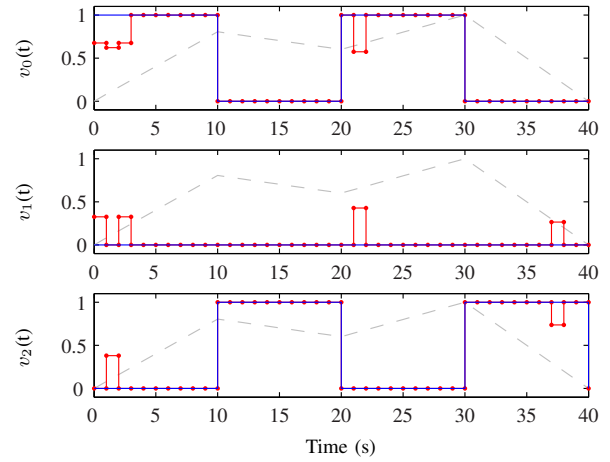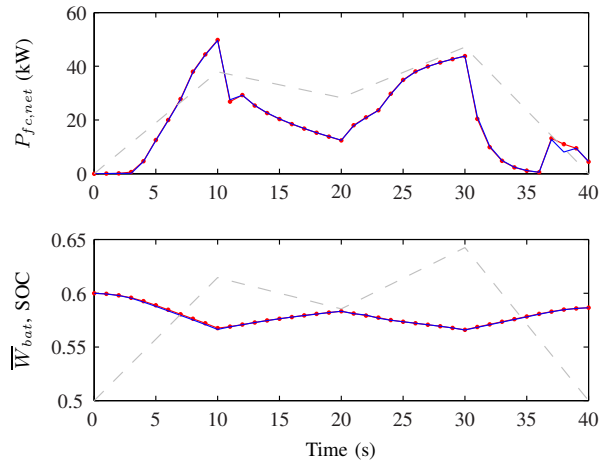 0, propelling/discharging. While the vehicle is slowing on [10,20]s and [30,40]s, the control takes advantage of excess kinetic and chemical energy (from a reduced propelling power need) to charge the battery, depleted during acceleration. During mode projection, the applied mode's N^i is at least two orders of magnitude greater than the rest on [0,3]s and five times greater on [21,22]s and [37,38]s.

The FCS net power and battery SOC evolution are given in Fig. 8. Here the fuel cell power has two definitive peaks that correspond to the drive cycle velocity peaks at 10 and 30 s. In contrast to the trapezoidal data, there is little variation between the embedded problem and simulation FCS powers, probably due to the large differences in N^i and the isolated use of mode projection. As with the trapezoidal profile results, when battery SOC is high, it is the primary motive source and as the SOC falls, the FCS contribution increases. The simulation fuel economy achieved is 2.13 kg H$_2$/100 km with a final SOC of 0.5865, a 2.25% difference from $\overline{W}_{bat,des}$.

Finally, Fig. 9 shows the battery and frictional braking power. For the reference deceleration over 10 s to 20 s, frictional braking is not needed since the sum of the FCS and EDS generated powers does not reach the battery's maximum charging power, i.e., does
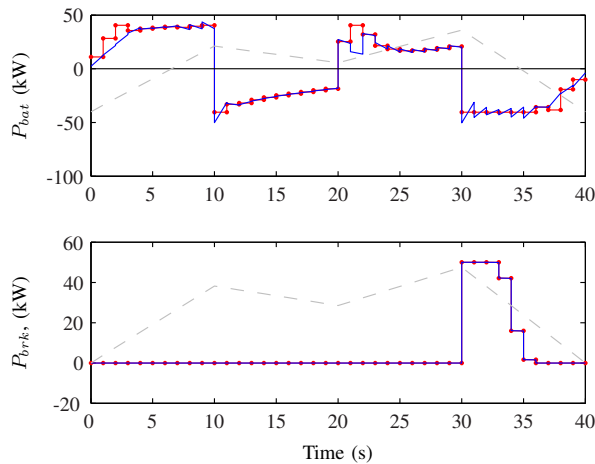
Fig. 9. Battery power (upper) and friction braking (lower) over the sawtooth drive cycle: (——) PEC simulation, (•) EOCP, (– –) superimposed drive profile.

not saturate the battery's ability to absorb excess power. However, at the beginning of the second, steeper reference velocity decrease on [30,40]s, the charging power is saturated and frictional braking is required. The 50 kW maximum braking power is applied for 3 s from the start of the interval. Reaching both the maximum charge power and braking implies no further deceleration can occur during this time. Again, the embedded problem and simulation battery powers are most different when mode projection is used since battery power is a function of the FCS and EDS control inputs, both of which change with projection.

3) Performance Cost Trade-Offs: As mentioned earlier, the weights in the EOCP cost function trade off conflicting requirements such as minimum fuel usage with minimum battery discharging. To illustrate this, C_{H_2} was increased to 200 while the other weights were left unchanged. Testing the trapezoidal drive profile results in a final SOC of 0.5798, 2-norm normalized velocity error of 1.00%, and 1.24 kg H_2/100 km fuel economy. The increased penalty on fuel usage leads to better fuel economy at the expense of battery SOC maintenance and velocity tracking. Conversely, doubling 2225 in the C_{bat} term gives a final SOC of 0.5939 with a fuel economy of 2.50 kg H_2/100 km and 2-norm normalized velocity error of 0.85%. The fuel economy and velocity tracking are degraded at the expense of battery SOC maintenance.

V. CONCLUSIONS

The EOCP mode embedding technique along with mode and control projection methods set forth herein have together been successfully applied in the context of MPC to the FCHV supervisory-level power flow control problem as demonstrated using two drive profiles. Three advantages result. First, traditional methods can be employed to solve the EOCP for the minimum PI cost and after projecting the controls onto the switched system, the cost is nearly equal to that of the EOCP. Second, the use of MPC allows the state measurements (through a detailed simulation) to keep errors from propagating. Third, by adjusting weights in the PI, trade-offs can be explored among vehicle velocity tracking, fuel economy, and battery health (SOC). These initial investigations gave good results with the same PI weights for the trapezoidal and sawtooth profiles. Future work will consider adding grade changes to the sawtooth profile, and exploration of the EPA drive cycles

and comparisons of these results to the Equivalent Consumption Minimization Strategy [2], [3]. ECMS presumes perfect drive cycle knowledge whereas we presume perfect state measurement and extrapolate the future velocity over the MPC horizon. Additional future work will focus on reducing the 3 s average EOCP solution time; an EOCP has been solved as fast as 50 μs [17].

REFERENCES

[1] C.-C. Lin, M.-J. Kim, H. Peng, and J. W. Grizzle, "System-level model and stochastic optimal control for a pem fuel cell hybrid vehicle," *Journal of Dynamic Systems, Measurement and Control, Transactions of the ASME*, vol. 128, no. 4, pp. 878 – 890, 2006. [Online]. Available: http://dx.doi.org/10.1115/1.2362785

[2] P. Rodatz, G. Paganelli, A. Sciarretta, and L. Guzzella, "Optimal power management of an experimental fuel cell/supercapacitor-powered hybrid vehicle," *Control Engineering Practice*, vol. 13, no. 1, pp. 41 – 53, 2005. [Online]. Available: http://dx.doi.org/10.1016/j.conengprac.2003.12.016

[3] L. Guzzella and A. Sciarretta, *Vehicle Propulsion Systems*, 2nd ed. New York, USA: Springer, 2007.

[4] A. Arce, A. J. del Real, and C. Bordons, "MPC for battery/fuel cell hybrid vehicles including fuel cell dynamics and battery performance improvement," *Journal of Process Control*, vol. 19, no. 8, pp. 1289 – 1304, 2009. [Online]. Available: http://dx.doi.org/10.1016/j.jprocont.2009.03.004

[5] S. C. Bengea and R. A. DeCarlo, "Optimal control of switching systems," *Automatica*, vol. 41, no. 1, pp. 11 – 27, 2005. [Online]. Available: http://dx.doi.org/10.1016/j.automatica.2004.08.003

[6] J. T. Pukrushpan, A. G. Stefanopoulou, and H. Peng, *Control of Fuel Cell Power Systems: Principles, Modeling, Analysis and Feedback Design*, 1st ed., ser. Advances in Industrial Control. London, England: Springer-Verlag Limited, 2004.

[7] R. T. Meyer and B. Yao, "Modeling and simulation of a modern PEM fuel cell system," *Proceedings of 4th International ASME Conference on Fuel Cell Science, Engineering and Technology, FUELCELL2006*, vol. 2006, 2006.

[8] K. Uthaichana, R. A. DeCarlo, S. C. Bengea, S. Pekarek, and M. Zefran, "Hybird optimal theory and predicitive control for power management in hybrid electric vehicle," *To appear in Journal of Nonlinear Systems and Applications*, 2011.

[9] R. Bartholomaeus, A. Fischer, and M. Klinger, "Real-time predictive control of hybrid fuel cell drive trains," in *Proceedings for the Fifth IFAC Symposium on Advances in Automotive Control*, Aptos, CA, United States, 2007.

[10] K. Uthaichana, "Modeling and control of a parallel hybrid electric vehicle," Ph.D. dissertation, Purdue University, 2006.

[11] V. Agarwal, K. Uthaichana, R. DeCarlo, and L. H. Tsoukalas, "Development and validation of a battery model useful for discharging and charging power control and lifetime estimation," *IEEE PES Transactions on Energy Conversion*, 2010.

[12] V. H. Johnson and T. Sack, "Temperature-dependent battery models for high-power lithium-ion batteries," in *17th Electric Vehicle Symposium*. Montreal, Quebec, Canada: World Electric Vehicle Association, 2000.

[13] T. Markel, A. Brooker, T. Hendricks, V. Johnson, K. Kelly, B. Kramer, A. O'Keefe, S. Sprik, and K. Wipke, "Advisor: a systems analysis tool for advanced vehicle modeling," *Journal of Power Sources*, vol. 110, no. 2, pp. 255 – 66, 2002/08/22. [Online]. Available: http://dx.doi.org/10.1016/S0378-7753(02)00189-1

[14] UQM Technologies, "PowerPhase 100," 2010, http://www.uqm.com/propulsion_specs.php.

[15] R. A. DeCarlo and R. Saeks, *Interconnected Dynamical Systems*. New York, USA: Marcel Dekker, Inc., 1981.

[16] S. Wei, K. Uthaichana, M. Žefran, R. DeCarlo, and S. Bengea, "Applications of numerical optimal control to nonlinear hybrid systems," *Nonlinear Analysis: Hybrid Systems*, vol. 1, pp. 264 – 279, 2007.

[17] J. Neely, S. Pekarek, and R. DeCarlo, "Hybrid optimal-based control of a boost converter," in *IEEE Applied Power Electronics Conference and Exposition*, 2009, pp. 1129–1127.

[18] F. Oettmeier, J. Neely, S. Pekarek, R. DeCarlo, and K. Uthaichana, "MPC of switching in a boost converter using a hybrid state model with a sliding mode observer," *IEEE Transactions on Industrial Electronics*, vol. 56, no. 9, pp. 3453–3466, 2009.